Topological Magnons with Nodal-Line and Triple-Point Degeneracies: Implications for Thermal Hall Effect in Pyrochlore Iridates

Kyusung Hwang, Nandini Trivedi, and Mohit Randeria
Department of Physics, The Ohio State University, Columbus, Ohio 43210, USA

(Received 26 November 2018; revised 19 December 2019; accepted 29 June 2020; published 22 July 2020)

We analyze the magnon excitations in pyrochlore iridates with all-in-all-out (AIAO) antiferromagnetic order, focusing on their topological features. We identify the magnetic point group symmetries that protect the nodal-line band crossings and triple-point degeneracies that dominate the Berry curvature. We find three distinct regimes of magnon band topology, as a function of the ratio of Dzyaloshinskii-Moriya interaction to the antiferromagnetic exchange. We show how the thermal Hall response provides a unique probe of the topological magnon band structure in AIAO systems.

DOI: 10.1103/PhysRevLett.125.047203

Introduction.—Recently there has been an explosion of activity exploring topological features in the electronic excitations of semimetallic and conducting solids. This includes the study of Weyl fermions in systems that break either time reversal or inversion symmetry [1–9]. Dirac fermions are realized by doubly degenerate band crossings protected by time reversal and crystal symmetries [10–16]. Recently discovered triple-point semimetals [17–22] are examples of new types of fermions, beyond Weyl and Dirac, with no counterpart in high energy physics. Nodal-line semimetals are another class of topological systems in which band crossings occur along closed lines in momentum space [23–27].

Topological semimetal band structures are not restricted to fermionic systems and can also arise in bosonic systems. Spin-orbit coupled magnetic insulators are good candidates to look for "bosonic" topological semimetals. In recent studies, a variety of topological features have been predicted in the magnon bands of Cr-based breathing pyrochlore antiferromagnets [28], pyrochlore ferromagnet $Lu_2V_2O_7$ [29], as well as other magnetic insulators [30–41].

In this Letter, we propose that the magnon excitations of pyrochlore iridates $R_2Ir_2O_7$ (R: rare earth or yttrium) [42,43] exhibit triple-point and nodal-line band crossings with unique signatures in thermal Hall effect. Many pyrochlore iridates are insulators with the all-in-all-out (AIAO) antiferromagnetic order [Fig. 1(a)] below $T_c \sim 120$ K [3,44–82]. Their spin excitations are relatively less explored experimentally due to neutron absorption by Ir. Focusing on compounds with nonmagnetic rare earth ion on the R site, such as $Eu_2Ir_2O_7$ and $Y_2Ir_2O_7$, we investigate the magnon excitations in the AIAO state described by the magnetic interactions between the $S = 1/2$ Ir moments on the pyrochlore lattice:

$$H = \sum_{\langle ij \rangle} [J\mathbf{S}_i \cdot \mathbf{S}_j + D\hat{d}_{ij} \cdot \mathbf{S}_i \times \mathbf{S}_j]. \tag{1}$$

We consider antiferromagnetic (AFM) Heisenberg exchange $J > 0$ and Dzyaloshinskii-Moriya (DM) interactions D between nearest-neighbor moments that are relevant for AIAO ordering (ferromagnetic exchange is relevant for $Lu_2V_2O_7$ [29,83,84]). We find two topological transitions in the magnon spectrum with increasing D/J as shown in Fig. 1(c). Interestingly, the three regimes

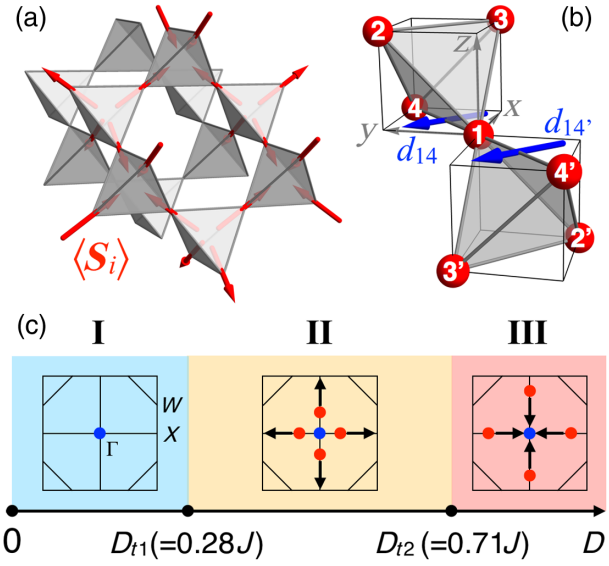

FIG. 1. (a) Spin configuration of the AIAO state on the pyrochlore lattice. (b) Nearest-neighbor DM vectors (blue), $\hat{d}_{14} = \hat{d}_{14'} = (-1, 1, 0)/\sqrt{2}$. The unit-length DM vectors $\{\hat{d}_{ij}\}$ are determined by lattice symmetry [91]. The numbers (1–4) denote the four sublattices of the pyrochlore lattice. (c) Three regimes (I,II,III) of magnon band topology separated by transition points D_{t1} and D_{t2}, showing magnon triple points (blue: A type, red: B type) in the $k_z = 0$ plane of the Brillouin zone [Fig. 2(d)]. Black arrows indicate the directions in which the triple points move with increasing D.

(I,II,III) can be distinguished by their distinct magnon band topology: the triply degenerate crossings of magnon bands [85], protected by the magnetic point group symmetry of the AIAO state, and nodal lines of doubly degenerate band crossings protected by either nonsymmorphic or antiunitary symmetries. The degeneracies at the triple points and nodal lines make strong contributions to the Berry curvature, which in turn impact the thermal Hall effect (THE) [83,84,86–90], an important experimental probe of magnon band topology.

Model and spin wave theory.—For the AFM pyrochlore described by Eq. (1), the DM interaction plays an important role in selecting the ground state from the highly degenerate ground state manifold in the Heisenberg limit. We focus on $D > 0$ (direct DM), where the ground state is AIAO, whereas for $D < 0$ (indirect DM) the ground state has XY order [69,91]. In the AIAO state relevant to the pyrohclore iridates, the spin moments point inward at one type of tetrahedra and outward at the other type [Fig. 1(a)] with ordering wave vector $\mathbf{q} = \mathbf{0}$.

We investigate magnon excitations about the AIAO state using linear spin wave theory. First, we make a local coordinate transformation for each spin operator that aligns the quantization axis along the moment direction at each site. Then, we use a linearized Holstein-Primakov transformation [92] to obtain the quadratic Hamiltonian

$$H_{\mathrm{SW}} = E_{\mathrm{cl}} + \sum_{\mathbf{k}} \sum_{l,m=1}^{4} A_{lm}(\mathbf{k}) a^{\dagger}_{l\mathbf{k}} a_{m\mathbf{k}} + \sum_{\mathbf{k}} \sum_{l,m=1}^{4} B_{lm}(\mathbf{k}) a_{l-\mathbf{k}} a_{m\mathbf{k}} + \mathrm{H.c.} \qquad (2)$$

Here E_{cl} is the classical ground state energy, and $a^{\dagger}$ (a) are the magnon creation (annihilation) operators for the four magnetic sublattices ($l, m = 1, \ldots, 4$) of the AIAO state with crystal momentum ($\mathbf{k}$). The explicit forms of the hopping and pairing amplitudes, $A_{lm}(\mathbf{k})$ and $B_{lm}(\mathbf{k})$, are provided in the Supplemental Material [93]. The corresponding four magnon bands are obtained by diagonalizing H_{SW} via the Bogoliubov transformation [93]. We next discuss in turn the two types of topological features in the magnon bands: triple points and nodal lines.

Triply degenerate crossings.—We find that the magnon bands exhibit two types of triply degenerate crossings (TDC); see Fig. 2(a). The first type is a triple degeneracy at the Γ point (blue dot) that we denote as the A-type TDC. It is protected by cubic symmetry (C_3 and C_2 rotations) [93] and exists irrespective of the size of D.

At $D = D_{t1}(\equiv J\sqrt{2}/5 = 0.28J)$ there is a band inversion at the Γ point between the triply degenerate level and nondegenerate level, resulting in the creation of a second B-type TDC [red dot in Fig. 2(b)]. The B-type TDC arises from the crossing between a nondegenerate and doubly degenerate (cyan) bands along the 6 cubic directions,

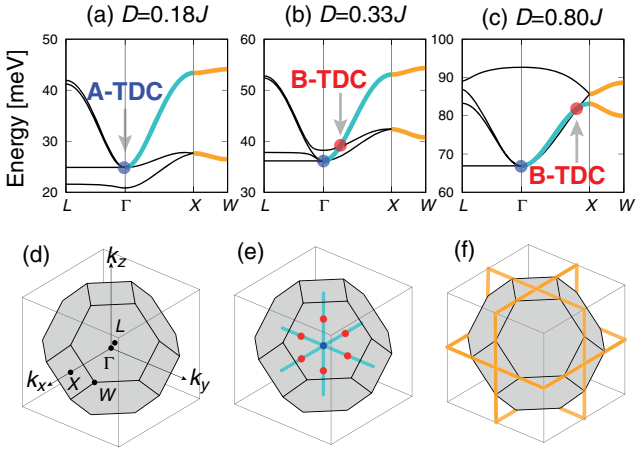

Band crossing	Location	Symmetry protection
A-TDC (blue)	Γ	$\{C_3, C_2\}$
B-TDC (red)	ΓX	Inverted bands at Γ & $\Theta * S_4$
Nodal-line (cyan)	ΓX	$\Theta * S_4$
Nodal-line (orange)	XW	$\{G_d, C_2\}$

FIG. 2. Magnon band structures for (a) $D = 0.18J$, (b) $0.33J$, and (c) $0.8J$. Two types of the triply degenerate band crossings are marked by blue (A-type TDC) and red (B-type TDC) dots. The cyan line denotes the doubly degenerate band protected by the $\Theta \cdot S_4$ antiunitary symmetry. The other doubly degenerate bands along XW (orange) correspond to the nodal-line band crossings protected by the nonsymmorphic G_d glide and C_2 rotation. (d) Brillouin zone of the pyrochlore lattice with high symmetry points [$\Gamma: (0,0,0)$, $X: (\pi/2,0,0)$, $W: (\pi/2,\pi/4,0)$, $L: (\pi/4,\pi/4,\pi/4)$]. (e)–(f) Locations of the triple points (e) and nodal lines (f) in the Brillouin zone, with the same color code as in (a)–(c). The table summarizes the associated symmetries protecting the band crossings. See the Supplemental Material [93] for the definitions of the symmetry operations.

e.g., ΓX line. The double degeneracy of the latter is guaranteed by the antiunitary symmetry $\Theta \cdot S_4$ of the magnetic point group of the AIAO state [93]. The B-type triple points move toward X and other symmetry related points as D increases. At $D = D_{t2}(\equiv J/\sqrt{2} = 0.71J)$ another band inversion arises at the X point. In this band inversion the TDC migrate to the bottom three bands from the top three with the inverted movement direction toward the Γ point [compare Figs. 2(c) with 2(b)]. During this process, a pair of triple points meet at the X point and then they pass through each other without being annihilated, due to the different quantum numbers of $(\Theta \cdot S_4)^2$ in the degenerate band (-1) and in the other two nondegenerate bands $(+1)$ along the $\mathbf{k}$ line.

To summarize, the AIAO antiferromagnetic pyrochlore has three regimes (I,II,III) of magnon band topology, separated by the topological transitions at D_{t1} and D_{t2}; see Fig. 1(c). The magnon band structure in each region is characterized by the pattern of triple points and their movement in the Brillouin zone. Note that the AIAO ground

TABLE I. Induced magnetization for several field directions, and resulting symmetry constraints on the thermal Hall conductivity tensor. The constraint for the [110] field direction holds for intermediate field directions between [110] and [111], i.e., $\hat{h} = (1/\sqrt{2})(\hat{x} + \hat{y})\cos\theta + \hat{z}\sin\theta$.

$\mathbf{h}$	$\mathbf{M} = (M_x, M_y, M_z)$	$\boldsymbol{\kappa} = (\kappa_{yz}, \kappa_{zx}, \kappa_{xy})$
[100]	$M_y = M_z = 0$	$\kappa_{zx} = \kappa_{xy} = 0$
[110]	$M_x = M_y$	$\kappa_{yz} = \kappa_{zx}$
[111]	$M_x = M_y = M_z$	$\kappa_{yz} = \kappa_{zx} = \kappa_{xy}$

state remains stable while the magnon band structure undergoes these topological changes driven by the DM interaction [93].

Nodal lines.—Another characteristic feature of the magnon bands is the existence of nodal-line band crossings. Along ΓX (cyan in Fig. 2) there is a doubly degenerate nodal-line band crossing. A more interesting nodal-line crossing occurs along the XW and other symmetry-related lines, where four magnon bands are paired up into two doubly degenerate bands [orange in Figs. 2(a)–2(c)] by the symmetry protection of C_2 rotation and "nonsymmorphic" G_d glide [93]. Acting on the magnon operators, these symmetry operations anticommute with each other, resulting in the double degeneracy. Figures 2(e) and 2(f) illustrate both kinds of nodal lines in the entire Brillouin zone.

We have examined the influence of symmetry-allowed further-neighbor interactions, beyond those included in Eq. (1), that may exist in real materials. We find that the essential features like the triple points and nodal lines are all preserved by symmetry, indicating that the qualitative features of THE persist in the presence of further-neighbor interactions [93].

Berry curvature and thermal Hall effect.—The distinct magnon band topology exhibited in the three regimes leads to qualitatively different patterns of Berry curvature in the band structure of each regime. A direct experimental signature of the magnon Berry curvature is the magnon thermal Hall effect [83,84,86–88]. A temperature gradient $\nabla_\nu T$ induces transverse heat current $J^Q_\mu = -\sum_\nu \kappa_{\mu\nu}\nabla_\nu T$ carried by magnon excitations as a result of their Berry curvature $\boldsymbol{\Omega}_{n\mathbf{k}} = (\Omega^x_{n\mathbf{k}}, \Omega^y_{n\mathbf{k}}, \Omega^z_{n\mathbf{k}})$. The antisymmetric thermal Hall conductivity tensor $\kappa_{\mu\nu}$ obtained from linear response theory is given by [88]

$$\kappa_{xy} = \frac{k_B^2 T}{\hbar V}\sum_{n=1}^{4}\sum_{\mathbf{k}}\left\{\frac{\pi^2}{3} - c_2[g(E_{n\mathbf{k}}/k_B T)]\right\}\Omega^z_{n\mathbf{k}}. \quad (3)$$

κ_{yz} and κ_{zx} are obtained by cyclic permutations of indices. Here $c_2(u) = (1+u)\{\ln[(1+u)/u]\}^2 - (\ln u)^2 - 2\mathrm{Li}_2(-u)$, with $\mathrm{Li}_2(x)$ the dilogarithm function, $g(x) = (e^x - 1)^{-1}$ is the Bose distribution, $E_{n\mathbf{k}}$ the magnon dispersion, and V the volume of the system. For each magnon band, the Berry curvature is given by [88,93]

$$\boldsymbol{\Omega}_{n\mathbf{k}} = i\sum_{m=1}^{8}\frac{\partial[T^{-1}_{\mathbf{k}}]_{nm}}{\partial\mathbf{k}} \times \frac{\partial[T_{\mathbf{k}}]_{mn}}{\partial\mathbf{k}}, \quad (4)$$

where $T_{\mathbf{k}}$ is the 8×8 Bogoliubov transformation matrix corresponding to the four bands and two "particle-hole" degrees of freedom.

To probe magnon Berry curvature via the thermal Hall effect, we apply a small magnetic field, which breaks time reversal and also breaks the cubic symmetry of the system. The Zeeman coupling $H_Z = -\mathbf{h}\cdot\sum_i \mathbf{S}_i$ generates a sublattice-dependent potential in the spin wave Hamiltonian H_{SW} and canting of the AIAO spin configuration (thereby a nonzero magnetization) [93]. In Table I, we summarize the direction of induced magnetization for several field directions, and also symmetry constraints on the thermal Hall conductivity tensor. The constraints are based on (i) remaining symmetries in the canted AIAO state under the field, and (ii) the fact that the tensor $\boldsymbol{\kappa} = (\kappa_{yz}, \kappa_{zx}, \kappa_{xy})$ and magnetization $\mathbf{M} = (M_x, M_y, M_z)(\equiv \frac{1}{4}\sum_{i=1}^{4}\langle\mathbf{S}_i\rangle)$ over a unit cell are both axial vectors that follow the same transformation rules under symmetry operations.

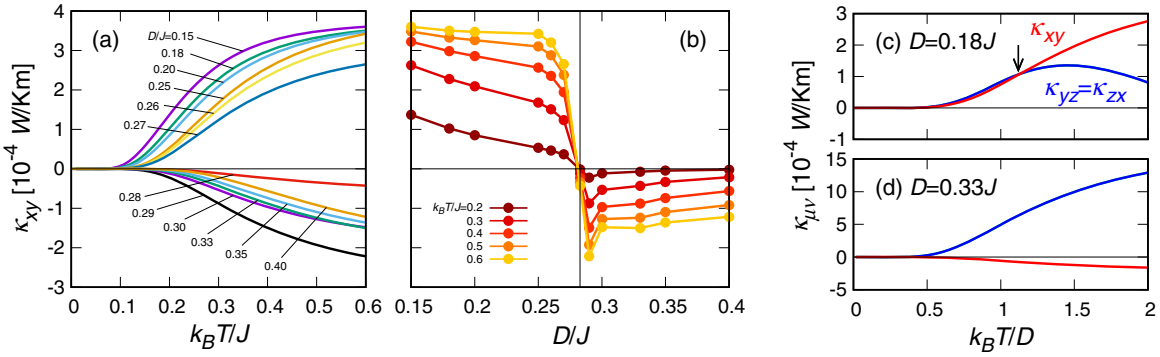

FIG. 3. Thermal Hall conductivity $\kappa_{\mu\nu}$ under a small magnetic field $h = 0.02J$ along the [110] direction. (a),(b) κ_{xy} as a function of T and D. The vertical line in (b) corresponds to D_{t1}. (c),(d) κ_{xy} (red) and $\kappa_{yz} = \kappa_{zx}$ (blue) for $D = 0.18J$ and $D = 0.33J$. The arrow in (c) indicates the crossing between κ_{xy} and κ_{yz} for $k_B T \approx D$.

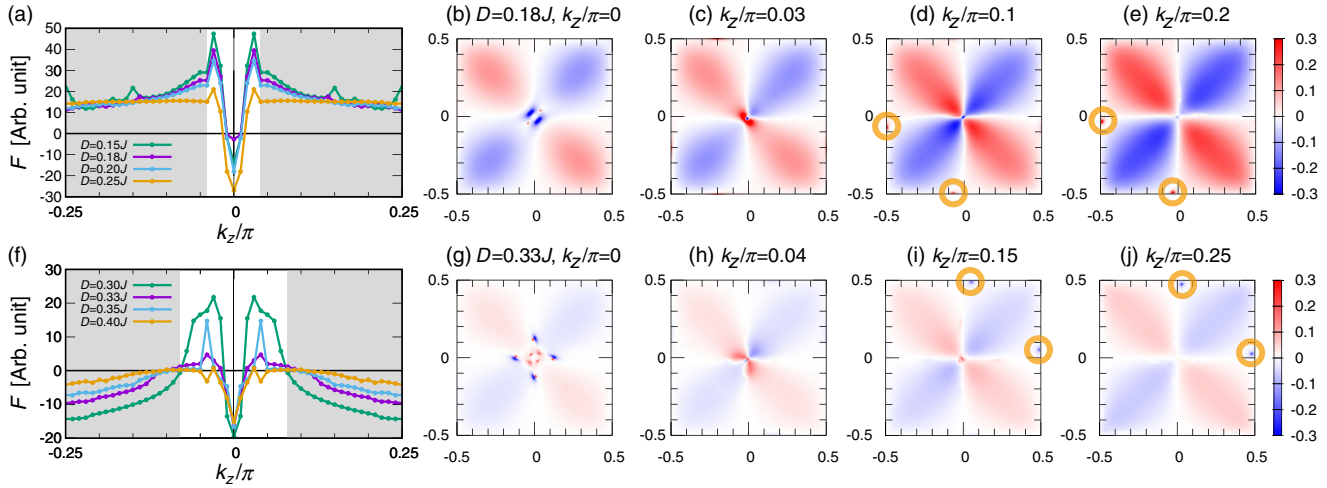

FIG. 4. Momentum-resolved thermal Hall conductivity $K_{xy}(\mathbf{k})$ at $k_BT = 0.3J$ under an applied field $h = 0.02J//[110]$. Left: $F = \int_{-\pi/2}^{\pi/2} dk_x \int_{-\pi/2}^{\pi/2} dk_y K_{xy}(\mathbf{k})$ as a function of k_z for (a) regime I and (f) regime II. Right: color map of K_{xy} for different k_z slices for (b)–(e) $D = 0.18J$ and (g)–(j) $D = 0.33J$. In each map, the horizontal and vertical axes represent k_x/π and k_y/π, respectively. See the text for an explanation of the shaded gray regions and orange circles.

We estimate the parameters of our model from resonant inelastic x-ray scattering experiments [65] on $Sm_2Ir_2O_7$ that show magnetic excitations well described by Eq. (1) with $J = 27.3$ meV and $D = 0.18J = 4.9$ meV. We use $J = 27.3$ meV to compute the thermal Hall effect, and examine our results as a function of D/J. We note that recent estimates [94] suggest that large D/J are achievable in pyrochlore iridates.

In Fig. 3, we show $\kappa_{\mu\nu}$ with a small field $h = 0.02J$ along the [110] direction, for which the relationship between magnon band topology and thermal Hall response is most clearly observed. The presence of a small field breaks all the symmetries listed in the table of Fig. 2. Instead, type-II Weyl points [95] are created from the A and B TDC as shown in Fig. 2.

The triple-point and nodal-line band crossings remain nearly degenerate carrying large Berry curvatures. We find characteristic behaviors in the thermal Hall conductivity that can help distinguish regimes I and II. Specifically, κ_{xy} has a different sign in the two regimes: positive in regime I and negative in regime II as shown in Fig. 3(a). In Fig. 3(b) we show that κ_{xy} changes sign across the boundary $D_{t1} = 0.28J$ (vertical line). The other two components ($\kappa_{yz} = \kappa_{zx}$) are positive below T_c, regardless of which regime the system lies in [Figs. 3(c) and 3(d)]. We find the same pattern of $\kappa_{\mu\nu}$ even upon inclusion of further neighbor interactions [93].

To get insight about the qualitatively different behavior of κ_{xy} in regimes I and II, we resolve it in momentum space: $\kappa_{xy} = (1/V)\sum_{\mathbf{k}} K_{xy}(\mathbf{k}) = \int_{-\pi/4}^{\pi/4} dk_z F(k_z)$. The k_z variation of the "integrated" quantity $F(k_z) \equiv \int_{-\pi/2}^{\pi/2} dk_x \int_{-\pi/2}^{\pi/2} dk_y K_{xy}(\mathbf{k})$, plotted in the left panels of Fig. 4, reveals important features of κ_{xy} in momentum space: (i) a peak structure around $k_z = 0$ that changes sign (white), and (ii) monotonic behavior with no sign change away from the center (gray). These plots show that constructive contributions from the gray region determine the sign of κ_{xy} in each of the two regimes.

In the right panels of Fig. 4, we plot $K_{xy}(\mathbf{k})$ as a function of (k_x, k_y) for various k_z slices to gain a better understanding of how the degeneracies of the (zero-field) magnon spectrum impact the Berry curvature and hence the sign of κ_{xy}. The large and rapidly changing behavior of $F(k_z)$ near $k_z = 0$ is seen to arise from the Berry curvature concentrated around the triple points [Figs. 4(b), 4(c), 4(g), and 4(h)].

More importantly, the doubly degenerate nodal lines along XW contribute to the large positive (negative) $F(k_z)$

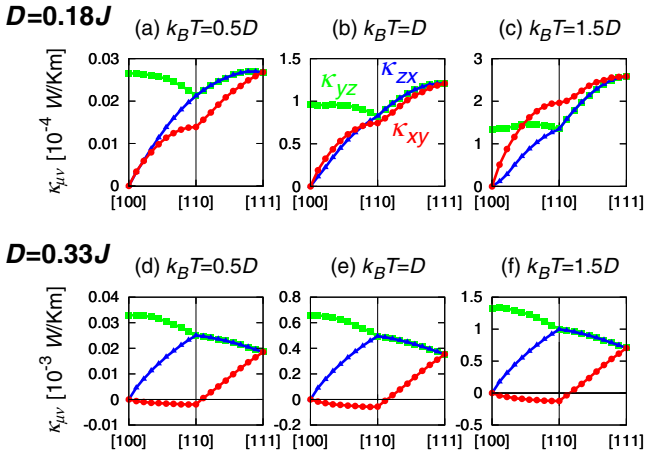

FIG. 5. Field-direction dependence of $\kappa_{\mu\nu}$ for $D = 0.18J$ (a)–(c) and $D = 0.33J$ (d)–(f). The horizontal axis represents the field direction $\hat{h}$ which changes from the [100] to [110] and then [111] direction, with the fixed magnitude $h = 0.02J$.

at large k_z in regime I (II). The peaks highlighted by circles in the right most panels correspond to the location of the degenerate energy levels [Figs. 4(d), 4(e), 4(i), and 4(j)]. In a small field, these levels are shifted from XW lines and their degeneracy is lifted, but only slightly, so they continue to give important contributions to $F(k_z)$. Notice that in regime I the nodal lines are shifted into the third quadrant of each k_z plane with positive $K_{xy}(\mathbf{k})$. By contrast, in regime II they move into the first quadrant with negative $K_{xy}(\mathbf{k})$. It is therefore the distinct field response of the nodal-line topological magnons that ultimately controls the sign of κ_{xy} in Fig. 3. The other nondegenerate bands generate the clover-leaf shaped "background" contributions in the right panels of Fig. 4.

From the above analysis, we see that different band topologies lead to distinct patterns of magnon Berry curvature, which in turn lead to different thermal Hall responses (see Fig. 3), indicating its usefulness as a probe of the overall magnon band topology.

The field-direction dependence of $\kappa_{\mu\nu}$ provides additional information about the two regimes, as depicted in Fig. 5 for two values of $D = 0.18J$ and $D = 0.33J$. We find (i) $\kappa_{xy} \geq 0$ in regime I but becomes negative along [100] to [110] in regime II. (ii) In regime I, κ_{xy} and κ_{zx} cross as the temperature drops below D regardless of the field direction [Figs. 5(a)–5(c)]. This generic crossing behavior can be useful for estimating the size of the DM coupling in thermal Hall experiments.

Conclusions.—One of the central ideas explored here is the field response of the topological magnon nodal lines and triple points and their manifestation in the thermal Hall transport. Going forward, our calculations suggest that pump-probe techniques that can excite magnons near the doubly and triply degenerate energy levels will lead to enhanced thermal Hall effect compared to simply relying on thermally excited magnons. Our calculations of the thermal Hall transport can also be extended to pyrochlore iridates with a magnetic rare earth ion [96] (such as $Nd_2Ir_2O_7$) with an additional magnetic ion.

This work was supported by NSF Materials Research Science and Engineering Center (MRSEC) Grants No. DMR-1420451 and No. DMR-2011876.

[1] O. Vafek and A. Vishwanath, Annu. Rev. Condens. Matter Phys. **5**, 83 (2014).
[2] N. P. Armitage, E. J. Mele, and A. Vishwanath, Rev. Mod. Phys. **90**, 015001 (2018).
[3] X. Wan, A. M. Turner, A. Vishwanath, and S. Y. Savrasov, Phys. Rev. B **83**, 205101 (2011).
[4] A. A. Burkov and L. Balents, Phys. Rev. Lett. **107**, 127205 (2011).
[5] K.-Y. Yang, Y.-M. Lu, and Y. Ran, Phys. Rev. B **84**, 075129 (2011).
[6] S.-Y. Xu *et al.*, Science **349**, 613 (2015).
[7] S.-M. Huang, S.-Y. Xu, I. Belopolski, C.-C. Lee, G. Chang, B. Wang, N. Alidoust, G. Bian, M. Neupane, C. Zhang, S. Jia, A. Bansil, H. Lin, and M. Z. Hasan, Nat. Commun. **6**, 7373 (2015).
[8] H. Weng, C. Fang, Z. Fang, B. A. Bernevig, and X. Dai, Phys. Rev. X **5**, 011029 (2015).
[9] B. Q. Lv, H. M. Weng, B. B. Fu, X. P. Wang, H. Miao, J. Ma, P. Richard, X. C. Huang, L. X. Zhao, G. F. Chen, Z. Fang, X. Dai, T. Qian, and H. Ding, Phys. Rev. X **5**, 031013 (2015).
[10] Z. Wang, Y. Sun, X.-Q. Chen, C. Franchini, G. Xu, H. Weng, X. Dai, and Z. Fang, Phys. Rev. B **85**, 195320 (2012).
[11] Z. Wang, H. Weng, Q. Wu, X. Dai, and Z. Fang, Phys. Rev. B **88**, 125427 (2013).
[12] B.-J. Yang and N. Nagaosa, Nat. Commun. **5**, 4898 (2014).
[13] M. Kargarian, M. Randeria, and Y.-M. Lu, Proc. Natl. Acad. Sci. U.S.A. **113**, 8648 (2016).
[14] Z. K. Liu, J. Jiang, B. Zhou, Z. J. Wang, Y. Zhang, H. M. Weng, D. Prabhakaran, S.-K. Mo, H. Peng, P. Dudin, T. Kim, M. Hoesch, Z. Fang, X. Dai, Z. X. Shen, D. L. Feng, Z. Hussain, and Y. L. Chen, Nat. Mater. **13**, 677 (2014).
[15] S.-Y. Xu, C. Liu, S. K. Kushwaha, R. Sankar, J. W. Krizan, I. Belopolski, M. Neupane, G. Bian, N. Alidoust, T.-R. Chang, H.-T. Jeng, C.-Y. Huang, W.-F. Tsai, H. Lin, P. P. Shibayev, F.-C. Chou, R. J. Cava, and M. Z. Hasan, Science **347**, 294 (2015).
[16] Z. K. Liu, B. Zhou, Z. J. Wang, H. M. Weng, D. Prabhakaran, S.-K. Mo, Y. Zhang, Z. X. Shen, Z. Fang, X. Dai, Z. Hussain, and Y. L. Chen, Science **343**, 864 (2014).
[17] Z. Zhu, G. W. Winkler, Q. S. Wu, J. Li, and A. A. Soluyanov, Phys. Rev. X **6**, 031003 (2016).
[18] H. Weng, C. Fang, Z. Fang, and X. Dai, Phys. Rev. B **93**, 241202(R) (2016).
[19] H. Weng, C. Fang, Z. Fang, and X. Dai, Phys. Rev. B **94**, 165201 (2016).
[20] B. Bradlyn, J. Cano, Z. Wang, M. G. Vergniory, C. Felser, R. J. Cava, and B. A. Bernevig, Science **353**, aaf5037 (2016).
[21] G. Chang, S.-Y. Xu, S.-M. Huang, D. S. Sanchez, C.-H. Hsu, G. Bian, Z.-M. Yu, I. Belopolski, N. Alidoust, H. Zheng, T.-R. Chang, H.-T. Jeng, S. A. Yang, T. Neupert, H. Lin, and M. Z. Hasan, Sci. Rep. **7**, 1688 (2017).
[22] B. Q. Lv, Z.-L. Feng, Q.-N. Xu, X. Gao, J.-Z. Ma, L.-Y. Kong, P. Richard, Y.-B. Huang, V. N. Strocov, C. Fang, H.-M. Weng, Y.-G. Shi, T. Qian, and H. Ding, Nature (London) **546**, 627 (2017).
[23] A. A. Burkov, M. D. Hook, and Leon Balents, Phys. Rev. B **84**, 235126 (2011).
[24] C. Fang, Y. Chen, H.-Y. Kee, and L. Fu, Phys. Rev. B **92**, 081201(R) (2015).
[25] Y. Chen, Y.-M. Lu, and H.-Y. Kee, Nat. Commun. **6**, 6593 (2015).
[26] Y. Chen, H.-S. Kim, and H.-Y. Kee, Phys. Rev. B **93**, 155140 (2016).
[27] G. Bian *et al.*, Nat. Commun. **7**, 10556 (2016).
[28] F.-Y. Li, Y.-D. Li, Y. B. Kim, L. Balents, Y. Yu, and G. Chen, Nat. Commun. **7**, 12691 (2016).
[29] A. Mook, J. Henk, and I. Mertig, Phys. Rev. Lett. **117**, 157204 (2016).

[30] J. Fransson, A. M. Black-Schaffer, and A. V. Balatsky, Phys. Rev. B **94**, 075401 (2016).
[31] Se Kwon Kim, Héctor Ochoa, Ricardo Zarzuela, and Yaroslav Tserkovnyak, Phys. Rev. Lett. **117**, 227201 (2016).
[32] S. A. Owerre, J. Phys. Condens. Matter **28**, 386001 (2016); J. Phys. Commun. **1**, 025007 (2017); Sci. Rep. **7**, 6931 (2017).
[33] N. Okuma, Phys. Rev. Lett. **119**, 107205 (2017).
[34] Y. Su, X. S. Wang, and X. R. Wang, Phys. Rev. B **95**, 224403 (2017).
[35] Y. Su and X. R. Wang, Phys. Rev. B **96**, 104437 (2017).
[36] K.-K. Li and J.-P. Hu, Chin. Phys. Lett. **34**, 077501 (2017).
[37] K. Li, C. Li, J. Hu, Y. Li, and C. Fang, Phys. Rev. Lett. **119**, 247202 (2017).
[38] S. A. Owerre, Phys. Rev. B **97**, 094412 (2018).
[39] V. A. Zyuzin and A. A. Kovalev, Phys. Rev. B **97**, 174407 (2018).
[40] S.-K. Jian and W. Nie, Phys. Rev. B **97**, 115162 (2018).
[41] S. A. Owerre, Europhys. Lett. **120**, 57002 (2017).
[42] W. Witczak-Krempa, G. Chen, Y. B. Kim, and L. Balents, Annu. Rev. Condens. Matter Phys. **5**, 57 (2014).
[43] R. Schaffer, E. K.-H. Lee, B.-J. Yang, and Y. B. Kim, Rep. Prog. Phys. **79**, 094504 (2016).
[44] D. Yanagishima and Y. Maeno, J. Phys. Soc. Jpn. **70**, 2880 (2001).
[45] N. Taira, M. Wakeshima, and Y. Hinatsu, J. Phys. Condens. Matter **13**, 5527 (2001).
[46] H. Fukazawa and Y. Maeno, J. Phys. Soc. Jpn. **71**, 2578 (2002).
[47] K. Matsuhira, M. Wakeshima, R. Nakanishi, T. Yamada, A. Nakamura, W. Kawano, S. Takagi, and Y. Hinatsu, J. Phys. Soc. Jpn. **76**, 043706 (2007).
[48] T. Hasegawa, N. Ogita, K. Matsuhira, S. Takagi, M. Wakeshima, Y. Hinatsu, and M. Udagawa, J. Phys. Conf. Ser. **200**, 012054 (2010).
[49] Y. Machida, S. Nakatsuji, S. Onoda, T. Tayama, and T. Sakakibara, Nature (London) **463**, 210 (2010).
[50] M. Sakata, T. Kagayama, K. Shimizu, K. Matsuhira, S. Takagi, M. Wakeshima, and Y. Hinatsu, Phys. Rev. B **83**, 041102(R) (2011).
[51] S. Zhao, J. M. Mackie, D. E. MacLaughlin, O. O. Bernal, J. J. Ishikawa, Y. Ohta, and S. Nakatsuji, Phys. Rev. B **83**, 180402(R) (2011).
[52] K. Matsuhira, M. Wakeshima, Y. Hinatsu, and S. Takagi, J. Phys. Soc. Jpn. **80**, 094701 (2011).
[53] K. Tomiyasu, K. Matsuhira, K. Iwasa, M. Watahiki, S. Takagi, M. Wakeshima, Y. Hinatsu, M. Yokoyama, K. Ohoyama, and K. Yamada, J. Phys. Soc. Jpn. **81**, 034709 (2012).
[54] S. M. Disseler, C. Dhital, T. C. Hogan, A. Amato, S. R. Giblin, C. de la Cruz, A. Daoud-Aladine, S. D. Wilson, and M. J. Graf, Phys. Rev. B **85**, 174441 (2012).
[55] S. M. Disseler, C. Dhital, A. Amato, S. R. Giblin, C. de la Cruz, S. D. Wilson, and M. J. Graf, Phys. Rev. B **86**, 014428 (2012).
[56] F. F. Tafti, J. J. Ishikawa, A. McCollam, S. Nakatsuji, and S. R. Julian, Phys. Rev. B **85**, 205104 (2012).
[57] M. C. Shapiro, S. C. Riggs, M. B. Stone, C. R. de la Cruz, S. Chi, A. A. Podlesnyak, and I. R. Fisher, Phys. Rev. B **85**, 214434 (2012).
[58] J. J. Ishikawa, E. C. T. O'Farrell, and S. Nakatsuji, Phys. Rev. B **85**, 245109 (2012).
[59] H. Sagayama, D. Uematsu, T. Arima, K. Sugimoto, J. J. Ishikawa, E. O'Farrell, and S. Nakatsuji, Phys. Rev. B **87**, 100403(R) (2013).
[60] H. Guo, K. Matsuhira, I. Kawasaki, M. Wakeshima, Y. Hinatsu, I. Watanabe, and Z.-a. Xu, Phys. Rev. B **88**, 060411(R) (2013).
[61] T. Kondo *et al.*, Nat. Commun. **6**, 10042 (2015).
[62] K. Ueda, J. Fujioka, B.-J. Yang, J. Shiogai, A. Tsukazaki, S. Nakamura, S. Awaji, N. Nagaosa, and Y. Tokura, Phys. Rev. Lett. **115**, 056402 (2015).
[63] Z. Tian, Y. Kohama, T. Tomita, H. Ishizuka, T. H. Hsieh, J. J. Ishikawa, K. Kindo, L. Balents, and S. Nakatsuji, Nat. Phys. **12**, 134 (2016).
[64] J. P. Clancy, H. Gretarsson, E. K. H. Lee, D. Tian, J. Kim, M. H. Upton, D. Casa, T. Gog, Z. Islam, B.-G. Jeon, K. H. Kim, S. Desgreniers, Y. B. Kim, S. J. Julian, and Y.-J. Kim, Phys. Rev. B **94**, 024408 (2016).
[65] C. Donnerer, M. C. Rahn, M. M. Sala, J. G. Vale, D. Pincini, J. Strempfer, M. Krisch, D. Prabhakaran, A. T. Boothroyd, and D. F. McMorrow, Phys. Rev. Lett. **117**, 037201 (2016).
[66] T. Fujita, Y. Kozuka, M. Uchida, A. Tsukazaki, T. Arima, and M. Kawasaki, Sci. Rep. **5**, 9711 (2015).
[67] T. Fujita, M. Uchida, Y. Kozuka, S. Ogawa, A. Tsukazaki, T. Arima, and M. Kawasaki, Appl. Phys. Lett. **108**, 022402 (2016).
[68] T. C. Fujita, M. Uchida, Y. Kozuka, W. Sano, A. Tsukazaki, T. Arima, and M. Kawasaki, Phys. Rev. B **93**, 064419 (2016).
[69] W. Witczak-Krempa and Y. B. Kim, Phys. Rev. B **85**, 045124 (2012).
[70] A. Go, W. Witczak-Krempa, G. S. Jeon, K. Park, and Y. B. Kim, Phys. Rev. Lett. **109**, 066401 (2012).
[71] E.-G. Moon, C. Xu, Y. B. Kim, and L. Balents, Phys. Rev. Lett. **111**, 206401 (2013).
[72] Eric Kin-Ho Lee, S. Bhattacharjee, and Y. B. Kim, Phys. Rev. B **87**, 214416 (2013).
[73] G. Chen and M. Hermele, Phys. Rev. B **86**, 235129 (2012).
[74] Q. Chen, H.-H. Hung, X. Hu, and G. A. Fiete, Phys. Rev. B **92**, 085145 (2015).
[75] H. Zhang, K. Haule, and D. Vanderbilt, Phys. Rev. Lett. **118**, 026404 (2017).
[76] R. Wang, A. Go, and A. J. Millis, Phys. Rev. B **95**, 045133 (2017).
[77] X. Hu, A. Rüegg, and G. A. Fiete, Phys. Rev. B **86**, 235141 (2012).
[78] B.-J. Yang and N. Nagaosa, Phys. Rev. Lett. **112**, 246402 (2014).
[79] Y. Yamaji and M. Imada, Phys. Rev. X **4**, 021035 (2014).
[80] X. Hu, Z. Zhong, and G. A. Fiete, Sci. Rep. **5**, 11072 (2015).
[81] K. Hwang and Y. B. Kim, Sci. Rep. **6**, 30017 (2016).
[82] P. Laurell and G. A. Fiete, Phys. Rev. Lett. **118**, 177201 (2017).
[83] Y. Onose, T. Ideue, H. Katsura, Y. Shiomi, N. Nagaosa, and Y. Tokura, Science **329**, 297 (2010).

[84] T. Ideue, Y. Onose, H. Katsura, Y. Shiomi, S. Ishiwata, N. Nagaosa, and Y. Tokura, Phys. Rev. B **85**, 134411 (2012).
[85] F-Y. Li and G. Chen, Phys. Rev. B **98**, 045109 (2018).
[86] H. Katsura, N. Nagaosa, and P. A. Lee, Phys. Rev. Lett. **104**, 066403 (2010).
[87] R. Matsumoto and S. Murakami, Phys. Rev. Lett. **106**, 197202 (2011); Phys. Rev. B **84**, 184406 (2011).
[88] R. Matsumoto, R. Shindou, and S. Murakami, Phys. Rev. B **89**, 054420 (2014).
[89] M. Hirschberger, R. Chisnell, Y. S. Lee, and N. P. Ong, Phys. Rev. Lett. **115**, 106603 (2015).
[90] H. Lee, J. H. Han, and P. A. Lee, Phys. Rev. B **91**, 125413 (2015).
[91] M. Elhajal, B. Canals, R. Sunyer, and C. Lacroix, Phys. Rev. B **71**, 094420 (2005).
[92] T. Holstein and H. Primakoff, Phys. Rev. **58**, 1098 (1940).
[93] See the Supplemental Material at http://link.aps.org/supplemental/10.1103/PhysRevLett.125.047203 for details of spin wave theory, symmetry analysis, magnon band structure, thermal Hall conductivity calculations, and influence of further-neighbor interactions.
[94] R. Yadav, M. Pereiro, N. A. Bogdanov, S. Nishimoto, A. Bergman, O. Eriksson, J. van den Brink, and L. Hozoi, Phys. Rev. Mater. **2**, 074408 (2018).
[95] A. A. Soluyanov, D. Gresch, Z. Wang, Q. Wu, M. Troyer, X. Dai, and B. A. Bernevig, Nature (London) **527**, 495 (2015).
[96] J. G. Rau, E. K.-H. Lee, and H.-Y. Kee, Annu. Rev. Condens. Matter Phys. **7**, 195 (2016).